

Broadband Thermal Imaging using Meta-Optics

Luocheng Huang¹, Zheyi Han¹, Anna
Wirth-Singh², Vishwanath Saragadam³, Saswata
Mukherjee¹, Johannes E. Fröch^{1,2}, Quentin A. A.
Tanguy¹, Joshua Rollag^{4,5}, Ricky Gibson⁵, Joshua R.
Hendrickson⁵, Phillip W.C. Hon⁶, Orrin Kigner⁶, Zachary
Coppens⁷, Karl F. Böhringer^{1,8}, Ashok Veeraraghavan³
and Arka Majumdar^{1,2*}

¹Department of Electrical and Computer Engineering, University
of Washington, Seattle, WA, USA.

²Department of Physics, University of Washington, Seattle, WA,
USA.

³Department of Electrical Engineering, Rice University,
Houston, TX, USA.

⁴KBR, Inc., 3725 Pentagon Blvd., Suite 210 Beaver Creek, OH,
USA.

⁵Sensors Directorate, Air Force Research Laboratory, 2241
Avionics Circle, Wright-Patterson AFB, OH, USA.

⁶NG Next, Northrop Grumman Corporation, 1 Space Park Drive,
Redondo Beach, CA, USA.

⁷CFD Research Corporation, Huntsville, AL, USA.

⁸Institute for Nano-Engineered Systems, University of
Washington, Seattle, WA, USA.

*Corresponding author(s). E-mail(s): arka@uw.edu;

Abstract

Subwavelength diffractive optics known as meta-optics have demonstrated the potential to significantly miniaturize imaging systems. However, despite impressive demonstrations, most meta-optical imaging systems suffer from strong chromatic aberrations, limiting their

utilities. Here, we employ inverse-design to create broadband meta-optics operating in the long-wave infrared (LWIR) regime (8-12 μm). Via a deep-learning assisted multi-scale differentiable framework that links meta-atoms to the phase, we maximize the wavelength-averaged volume under the modulation transfer function (MTF) of the meta-optics. Our design framework merges local phase-engineering via meta-atoms and global engineering of the scatterer within a single pipeline. We corroborate our design by fabricating and experimentally characterizing all-silicon LWIR meta-optics. Our engineered meta-optic is complemented by a simple computational backend that dramatically improves the quality of the captured image. We experimentally demonstrate a six-fold improvement of the wavelength-averaged Strehl ratio over the traditional hyperboloid metalens for broadband imaging.

Keywords: LWIR, inverse design, meta-optic, metasurface, broadband

1 Introduction

Long-wavelength infrared (LWIR) imaging is a critical key technology for non-contact thermography, long-range imaging, and remote sensing, with applications spanning consumer electronics to defense [1]. High resolution imaging in LWIR typically requires bulky, and precisely engineered refractive surfaces, which ultimately add to the overall volume and weight of the imaging system, especially for high numerical aperture (NA) optics. To reduce the size and weight of LWIR imagers, diffractive optical elements such as multi-level diffractive lenses (MDL)[2] have been used as an alternative to traditional refractive optics. However, the use of MDLs has been limited by the complexity of the multi-layer fabrication and the large periodicity, resulting in higher order diffraction. Sub-wavelength diffractive optics, also known as meta-optics, have recently generated strong interest to spatially modulate the phase, amplitude, and polarization of the incident wavefront. These consist of scatterers, which are placed on a sub-wavelength periodic lattice to avoid any higher order diffraction, whereas the active layer thickness of the device corresponds to the height of the scatterers [3–16]. Due to the drastic thickness and weight reduction in meta-optics compared to refractive lenses, LWIR meta-optical imaging under ambient light conditions have been recently reported [17–19]. However, until this point, the captured image quality remained relatively poor compared to refractive lenses, primarily due to strong chromatic aberrations.

Some drawbacks of meta-optics are inherited from their diffractive counterparts, the most significant one being their axial chromatic aberration. This happens because the phase wrapping condition for different wavelengths is met at different radii [13, 20]. The dispersion engineering approach can ameliorate this axial chromatic aberration to some degree, but ultimately faces fundamental limitations explicitly set by the achievable group delay and group

delay dispersion [21] for large aperture meta-optics. To overcome this fundamental limitation and enhance the image quality, chromatic aberrations in a large-aperture meta-optics can be mitigated via computational imaging using forward designed meta-optics that exhibit extended depth of focus (EDOF) properties, as demonstrated in the visible regime[22, 23].

However, for forward designed meta-optics an optical designer has to strongly rely on experience and intuition about the functionality of the meta-optics. As such, this method does not provide a clear path to further improve the imaging quality. Unlike forward design, inverse design approaches define the performance of the optical element via a figure of merit (FoM), and computationally optimize their structure or arrangement to maximize the respective FoM. The inverse design methodology has been very successful in creating non-intuitive yet functional meta-optics [24–26], including EDOF lenses for broadband imaging in the visible. A further refinement and extension of this approach is end-to-end design, where the meta-optics and computational backend are co-optimized with a FoM defined by the final image quality[27]. While such an approach takes the entire system into account, the downside is that we often lack the insight into how and why the optic performs well. This can be detrimental when translating designs from the visible domain (with ample training data) to the thermal domain (with paucity of training data). As such, a new design paradigm is required for meta-optical imagers, which provides intuition on why such meta-optics can perform broadband imaging.

In this paper, we report a 1 cm ($\sim 1000\lambda$) aperture, f/1 (numerical aperture (NA): 0.45) broadband polarization-insensitive LWIR meta-optics, designed by a multi-scale optimization technique that maximizes the wavelength-averaged volume under the modulation transfer function (MTF) of the meta-optic. This method is “multi-scale” as distinct computational methods are used to calculate the electric fields at different length scales. The meta-optics are implemented in an all-silicon platform and we demonstrate that the captured images exhibit superior performance over traditional hyperboloid metalens. Unlike previous works, which relied either on local engineering of meta-atoms (dispersion engineering) or global engineering of the phase-mask, our optimization technique employs both meta-atom and phase-mask engineering. We show that such an extended approach clearly outperforms a phase-mask engineering only approach.

2 Results

2.1 Inverse Design Framework

The key to achieve meta-optical broadband LWIR imaging is a fully-differentiable inverse design framework that optimizes the binary structures (i.e., binary permittivity distribution) of the meta-atoms to achieve focusing of the desired wavelengths (**Fig. 1(a)**). However, designing a large-area ($\sim 10^3\lambda$) meta-optic is a computationally prohibitive problem, and full-wave simulation is not possible. Therefore, phase-mask optimization is generally used, but

the scatterer-to-phase mapping on a sub-wavelength scale is not differentiable and a look-up-table based approach does not work for such an optimization methodology. In the past, polynomial proxy functions have been employed to connect scatterers to the corresponding phase [27], but were limited to only a monotonic relation. However, for broadband operations meta-atoms with a large phase diversity with multiple phase wrappings are required but suffer from multiple resonances at various wavelengths.

We solve this problem by utilizing a deep neural network (DNN)-based surrogate model, that maps the geometrical parameters ($\vec{\mathbf{p}}$) of the meta-atom to its complex transmission coefficient $\hat{\mathbf{E}}(\vec{\mathbf{p}}, \lambda)$. The utilization of DNNs enable modeling highly complex functions, which are well suited for broadband meta-optics. To emphasize this point, we compare meta-atoms with different degrees of parameterization: the “simple” scatterers are defined by one design parameter (the width of the pillar), whereas the “complex” scatterers have three parameters, see **Fig. 1**(b). For each type of meta-atom, we sampled the parameters $\vec{\mathbf{p}}$ uniformly for each feature dimension and simulated it using rigorous coupled wave analysis (RCWA) [28], across different wavelengths λ . The simulated meta-atom library is then taken as the training data set for the DNN that maps the parameterized features to the phase modulation. The RCWA simulations and the DNN fitting are pre-computed before the optimization loop, shown in **Fig. 1**(c). Although we are currently limited to parameterized meta-atoms, with the rapid progress of machine learning-enabled meta-optics design, we anticipate voxel-level meta-atom engineering will be possible in the near future. Also, our design currently relies on the local phase approximation, which is known to provide lower efficiency for meta-optics. However, recently a physics-inspired neural network has been used to design meta-optics without making such approximation and can be readily adapted for the scatterer-to-field mapping [29].

We define the FoM by computing the normalized MTFs first as $\hat{M}(k_x, k_y, \lambda, \theta)$, where k_x, k_y are defined as the spatial frequencies in the x and y direction, λ is the optical wavelength, and θ signifies the incident angle (more details in Methods). The modified Strehl Ratio \mathbf{S} can then be calculated using the following expression:

$$\begin{aligned} \mathbf{S}(\lambda, \theta) &= \int_{-k_{y1}}^{k_{y1}} \int_{-k_{x1}}^{k_{x1}} \hat{M}(k_x, k_y; \lambda, \theta) dk_x dk_y \\ &= \sum_i \sum_j \hat{M}(k_x(i), k_y(j); \lambda, \theta) \Delta k_x \Delta k_y \end{aligned} \quad (1)$$

Here, k_{x1} and k_{y1} denote the cutoff spatial frequencies in the x and y direction. Using the modified Strehl Ratio, the FoM \mathbf{F} is computed as:

$$\mathbf{F} = \log\left(\prod_i \prod_j S(\lambda_i, \theta_j)\right) \quad (2)$$

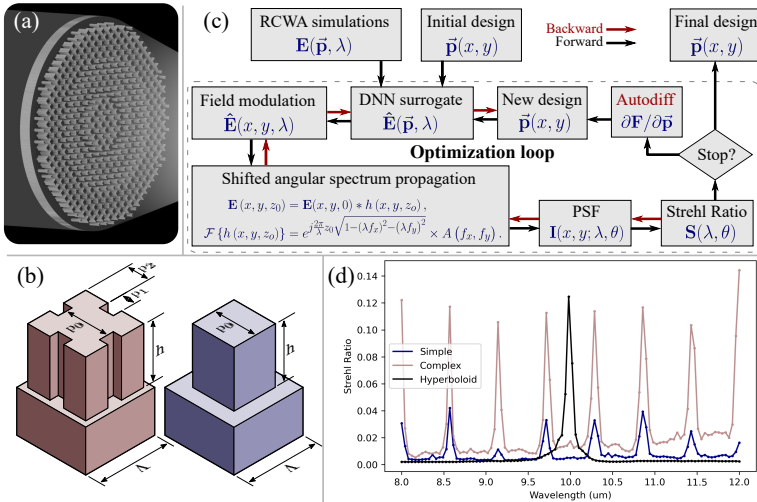


Fig. 1 Design methodology to create the broadband LWIR meta-optics. (a) Our objective is a LWIR meta-optic that focuses broadband light at the same focal plane. (b) Parameterization of the “complex” (red) and the “simple” (blue) scatterers. For the complex scatterers, three variable parameters control the binary profile, namely, \mathbf{p}_0 , \mathbf{p}_1 , and \mathbf{p}_2 . This method of parameterization ensures 4-fold symmetry of the geometry, thus ensuring polarization-insensitivity. The height \mathbf{h} is kept constant at $10\ \mu\text{m}$. The meta-atoms sit on a Manhattan grid with a periodicity \mathbf{A} set to $4\ \mu\text{m}$. (c) Block diagram of the optimization routine. (d) The simulated Strehl ratio of the “simple”, “complex”, and hyperboloid meta-optic.

This FoM can be interpreted as the wavelength and incidence angle-averaged volume under the MTF surface, and we therefore term this optimization routine as “MTF engineering”. We emphasize that our FoM is maximized when all individual $S(\lambda_i, \theta_j)$ are identical, thus constraining our meta-optics to have a uniform performance for the specified wavelengths without explicitly defining uniformity as an optimization criteria. Since the entirety of the forward computation of the FoM is implemented using differentiable operations, the gradient of the FoM with respect to the geometry parameters, i.e. $\partial\mathbf{S}/\partial\vec{\mathbf{p}}$, can be readily obtained using automatic differentiation through chain rule in the direction indicated by the red arrows in **Fig. 1**(b). A stochastic gradient descent algorithm then optimizes the structural parameters $\vec{\mathbf{p}}$. The optimization routine halts when the value of FoM converges, yielding the final meta-optic design.

2.2 Meta-optics Design

Using the “MTF engineering” framework, we designed the broadband LWIR meta-optics. We opted for an all-silicon platform, which is composed of silicon pillars on a silicon substrate, to simplify the fabrication process. We note that while silicon does absorb some of the LWIR light, we still expect about 80% light transmission.

In this study, we designed two different broadband meta-optics, each with a unique scatterer archetype shown in **Fig. 1**(b). Both archetypes were parameterized to ensure fourfold symmetry, which leads to polarization insensitivity. Additionally, we designed a hyperboloid metalens, based on a forward design approach [23], possessing similar height and periodicity, to serve as a baseline for comparison. All designed meta-optics have a nominal focal length of 1 cm and a numerical aperture of 0.45. In our simulations, the optimized broadband meta-optics displayed significantly larger wavelength-averaged Strehl Ratios—0.045 for the meta-optics with “complex” scatterers and 0.018 for those with “simple” scatterers, as compared to 0.0075 for the forward-designed hyperboloid metalens. The simulations were, however, limited to 8 optimized wavelengths spanning from 8 to 12 μm due to memory constraints. **Fig. 1**(d) depicts the simulated Strehl ratios of the optics described above in relation to the input wavelength. For these simulations, individual meta-atoms were simulated using RCWA, while DNN mapping was utilized solely for optimization. To mimic fabrication imperfections, we introduced normally distributed perturbation into each meta-atom’s design parameters. Remarkably, the complex meta-optic design yielded Strehl ratios at eight sampled wavelengths that are comparable to the Strehl ratio at a single operational wavelength of the hyperboloid metalens.

Although the spectral regions between the sampled wavelengths exhibit relatively lower Strehl ratios compared to the peak values, these ratios for the non-sampled wavelengths still remain significantly larger than those of the hyperboloid lens at the same wavelengths. As such, when averaged over all the wavelengths of interest, we still obtain a six-fold improvement for the average Strehl ratio. Our experimental results demonstrate that, despite such polychromatic behavior, it is possible to capture images under broadband ambient thermal radiation. This highlights the practicality and adaptability of our broadband meta-optic designs in real-world scenarios.

2.3 Fabrication

We fabricated the LWIR meta-optics in an all-silicon platform, with a set of devices shown in **Fig. 2**(a). We pattern the Si wafer with laser direct-write lithography and etch the patterns using deep reactive ion etching (details in Methods). We note that patterning can also be accomplished with a mask aligner – therefore our all-silicon platform can be adapted to large scale foundry processes. Scanning electron microscope images of the fabricated complex and simple meta-optics are depicted in **Fig. 2**(b) and **2**(c), respectively.

2.4 Imaging

We first characterized the PSF of the fabricated lenses (result in the Appendix), and observed less variation of the PSFs across the LWIR range as expected. To conclusively demonstrate that the MTF-engineered optics deliver superior imaging quality compared to the forward-designed metalens,

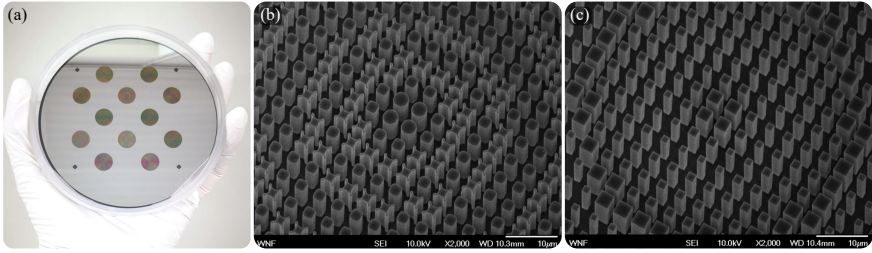


Fig. 2 Images of the fabricated meta-optics: (a) Camera image of a fabricated wafer with several meta-optics. SEM images of the meta-optics with (b) complex scatterers and (c) simple scatterers.

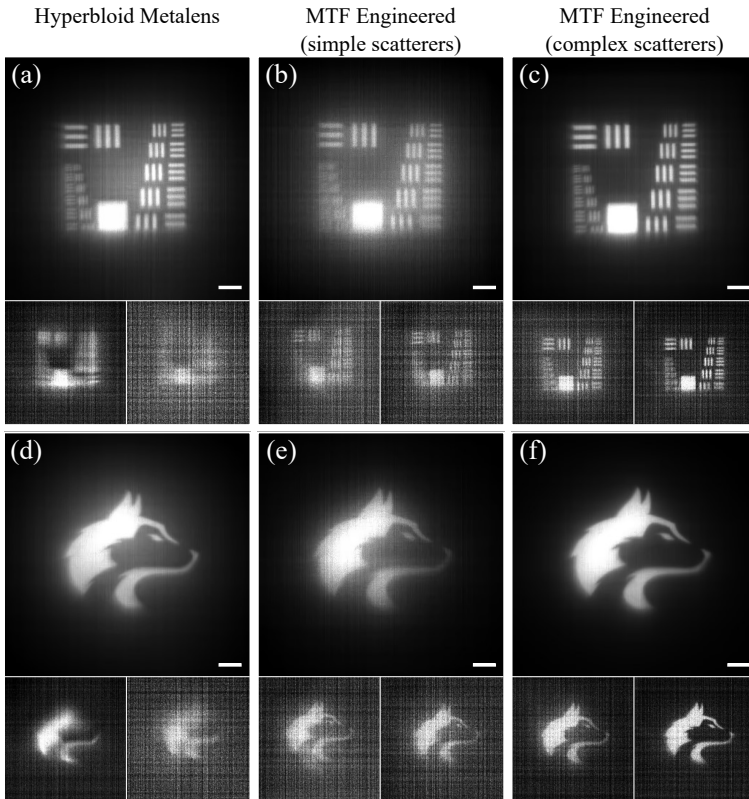


Fig. 3 Broadband imaging results in the lab (after computation), comparing the hyperboloid metalens (a, d), MTF engineered meta-optic with simple scatterers (b, e), and MTF engineered meta-optic with complex scatterers (c, f). For each subfigure the imaging results are shown without a filter (top), with a $10 \pm 0.25 \mu\text{m}$ bandpass filter (bottom left), and with a $12 \pm 0.25 \mu\text{m}$ bandpass (bottom right). The scale bar is 0.56 mm . Imaging results using two different targets, namely are a modified USAF 1951 pattern (top) and a picture of a husky (bottom) are shown.

we evaluated their respective imaging performance under controlled conditions (see Methods for details). As illustrated in **Fig. 3**, the images captured using the MTF-engineered meta-optic with complex scatterers exhibit the highest level of clarity and detail. Stripe elements of an imaging target can be clearly distinguished and well separated, emphasizing the overall crispness of the images.

To highlight the broadband capability of the MTF-engineered meta-optics, we captured images using both 10 μm and 12 μm bandpass filters (each with a linewidth of 500nm). We ensured a consistent distance between the meta-optics and the imaging sensor, maintaining a nominal operating wavelength of 11 μm . The resultant imaging outputs, which are presented without any denoising, are displayed at the bottom of each sub-figure in **Fig. 3**. Notably, the MTF-engineered meta-optic with complex scatterers outperforms both the simple scatterers and the forward-designed optics for both the line and husky targets. Additionally, the MTF-engineered meta-optic with simple scatterers demonstrates superior performance over the forward-designed hyperboloid metalens, as evidenced by a clearer image and higher peak signal-to-noise ratio (PSNR) for both patterns in both the 10 μm and 12 μm cases. A comprehensive list of PSNR values can be found in the Appendix.

To further emphasize the capabilities of the MTF-engineered LWIR meta-optics, we performed imaging “in the wild” under both indoor and outdoor ambient daylight conditions, shown in **Fig. 4**. In each case, we captured a single image using a FLIR A65 sensor, and performed a numerical deconvolution (details in the Methods and supplementary information). The MTF-engineered meta-optic with complex scatterers and forward-designed meta-optics were tested against a refractive lens for the ambient imaging, seen on **Fig. 4(a)**. First, we imaged a truck parked outdoors shown in **Fig. 4(b)**. The vehicle details are clearly visible such as the front grill, as well as background details, such as the windows on the top right corner of the image, and the stairs on the left side of the image captured using MTF-engineered meta-optic. In contrast, the hyperboloid image suffers from strong glowing artifacts in the center and fails to recover sharp details. **Fig. 4(c)** shows images of a parked car. As with the previous example, the details are clearly visible, including the tires on the car, and the branches of the tree in the background with the MTF-engineered lens. **Fig. 4(d)** shows image of a person with hands stretched out. The difference between MTF-engineered lens and hyperboloid metalens is distinctively visible here. The sharp image features are clearly visible in the MTF-engineered lens, including variable heat patterns on the shirt. In contrast, the image formed by the hyperboloid lens is noisy with no clear features on the person.

3 Discussion

In this work, we have devised an inverse design methodology for broadband imaging meta-optics, guided by readily translatable, intuitive, and universal

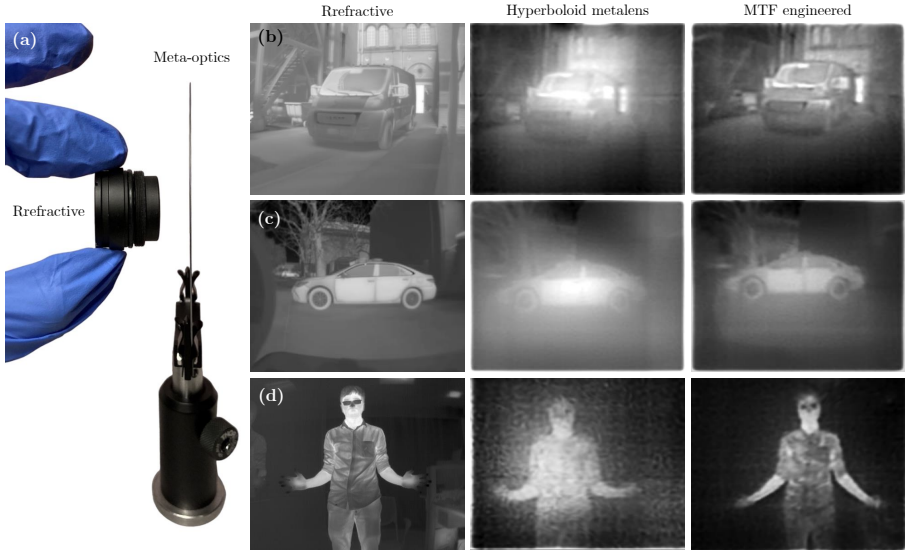


Fig. 4 LWIR imaging “in the wild”. (a) Thickness comparison between the refractive lens (left) and the meta-optics (right). Three scenes were imaged using the refractive LWIR lens (left), the hyperboloid metalens (middle), and the MTF engineered meta-optic with complex scatterers (right). Scenes (b) and (c) were captured outdoors on a sunny day while (d) was captured indoors.

objective function, given by the volume of a multi-chromatic MTF surface. Utilizing this MTF-engineering approach, we achieve a sophisticated, yet easily fabricable, large-aperture, broadband LWIR meta-optic, suitable for “in the wild” imaging under ambient temperature conditions. We have experimentally verified this framework and demonstrated polarization-insensitive broadband LWIR meta-optics with a diameter of 1 cm and NA of 0.45. While previous works based on forward designed LWIR meta-optics have demonstrated imaging capabilities [23], they fell short in resolving fine features due to strong chromatic aberrations. In contrast, our MTF-engineered meta-optics show significantly improved performance over a broadband spectral range, as well as narrowband imaging capabilities for wavelengths outside the center wavelength.

We further elucidate, both in simulation and experiment, how a significant performance enhancement can be achieved for MTF-engineered meta-optics if we consider more structural degrees of freedom. Such complex parameterization of the meta-optics broadens the solution space during the optimization process, thereby increasing the likelihood of achieving an improved FoM. This provides a clear pathway for future designs to leverage a performance boost by employing a higher degree of parameterization for the meta-optic scatterer, combined with large-scale optimization of the meta-optic. We note that previous works primarily employed either meta-atom engineering or phase-mask optimization, often overlooking potential synergistic effects. We demonstrate unequivocally that by utilizing structural diversity along with

global phase-mask engineering, a six-fold performance improvement can be achieved. However, a clear downside is that the sampling complexity increases exponentially with the number of structural parameters. Additionally, fabrication resolution requirements become more stringent with the increased complexity of the meta-atoms. Despite these challenges, they can potentially be overcome by using a more clever parameterization of the meta-atom, similar to what has been achieved in dispersion engineering approaches.

Overall, the developed MTF-engineering framework provides a universal methodology for creating large-area broadband meta-optics. Our imaging and characterization results clearly demonstrate the advantages of employing the MTF-engineering methodology over the traditional forward design. We showcase that the MTF-engineered flat optics open a new avenue for miniaturizing LWIR imaging systems, with potential applications in unmanned aerial vehicles, thermal scopes, and perimeter security.

4 Methods

4.1 MTF Calculation

Each meta-atom is assigned a position (x, y) on a Manhattan grid with a periodicity of $\mathbf{\Lambda}$ and a height of \mathbf{h} , whose geometric parameters are $\vec{\mathbf{p}}$. These geometric parameters are given random assigned initial values within the fabrication limited bounds. The spatial modulation of the meta-optic $\hat{\mathbf{E}}(x, y, \lambda)$ is calculated given the meta-atom position and the wavelengths of the incident fields. The spatial modulation is then multiplied by the incident field (planewave with incidence angle θ) and propagated to the sensor plane centered to the chief ray, using the shifted angular spectrum method [30]. The variable $I(x, y; \lambda, \theta)$ represents the sampled intensities on the sensor plane given all permutations of the wavelengths and angles of incidence of the incident fields. This intensity is the point spread function (PSF) of the imaging system. The MTF (M) is computed from the PSF given by $\mathbf{M}(k_x, k_y; \lambda, \theta) = |\mathcal{F}(I(x, y; \lambda, \theta))|$, where \mathcal{F} is the Fourier transform. The diffraction limited MTFs are denoted as $D(k_x, k_y, \lambda)$. The normalized MTF is defined as $\hat{M} = M(k_x, k_y, \lambda)/D(k_x, k_y, \lambda)$.

4.2 Optimization

For the design with the complex scatterer, we used 40 samples per feature dimension in $\vec{\mathbf{p}}$ while keeping h constant at 10 μm . Combining with 101 samples of wavelengths λ , there are totally $40^3 \times 101$ RCWA simulations conducted for training of the DNN model. For the simple scatterer case, we sampled 1000 values for the only structure variable p_1 and 101 wavelengths, also keeping h constant at 10 μm , resulting in 1000×101 training samples for the surrogate. For training the DNN surrogate model, the Adam optimizer is used with a learning rate of 10^{-3} for 1000 epochs. To span a diameter of 10 cm, a total

of 2500×2500 meta-atoms are used with a periodicity of $10 \mu\text{m}$. During optimization, a total of 13 samples of wavelengths are used uniformly spanning from $8 \mu\text{m}$ to $12 \mu\text{m}$. We selected 0° and 10° to be the angles of incidence in our optimization.

The DNN surrogate model uses four layers of fully connected layers that have 256 units and hyperboloid tangent as the activation function for each layer. To ensure a differentiable mapping, the fitted surrogate model uses all differentiable operations.

The structure parameters $\vec{\mathbf{p}}$ are assigned initial values within the fabrication limited bounds. There are two conditions for the optimization loop to halt: (1) $\vec{\mathbf{p}}$ converges, i.e. $\vec{\mathbf{p}}_n - \vec{\mathbf{p}}_{n-1} < \mathbf{T}$, where \mathbf{T} denotes a threshold, and n represents the iteration number; (2) the number iteration reaches a certain integer \mathbf{N} . When one halting conditions is met, the final meta-atom binary structure parameters are converted to GDSII files for fabrication.

4.3 Characterization

We characterized the PSFs of the fabricated meta-optics using a confocal microscopy setup in the LWIR. In this configuration, a tunable, $8.23 - 10.93 \mu\text{m}$, quantum cascade laser (QCL) with 500 ns pulses and repetition rate of 100 kHz (Daylight Solutions 31090-CT) was incident on a Ge aspheric lens with focal length $f_1=20$ mm and NA of 0.63 (Edmund Optics #68-253). This lens focused the QCL onto a $30 \mu\text{m}$ diameter pinhole (Thorlabs P30S) where approximately 30% of the incident power was transmitted. The QCL was then incident on the meta-optic, placed $2f_{meta} + f_2 = 35$ mm from the pinhole. The beam was then collimated by a Ge aspheric lens with $f_2=15$ mm and NA of 0.83 (Edmund Optics #68-252) placed $f_{meta} + f_2=35$ mm after the meta-optic. The beam then traveled to a ZnSe plano-convex lens with $f_3=50.8$ mm which focused the beam onto the image plane. This ZnSe lens was created by Rocky Mountain Instrument Co. and had a custom coating covering the $3 - 12 \mu\text{m}$ range with a reflectivity $R_{avg} \leq 5\%$. The image was captured on a strained layer superlattice (SLS) focal plane array (FPA) with a $15 \mu\text{m}$ pixel pitch and 640×512 pixels (FLIR A6751 SLS) cooled to 76 K. The camera acquisition time was $200 \mu\text{s}$ to best fit the 14-bit dynamic range of the FPA and 100 frames were captured and averaged with background correction. The schematic of the setup and the component specifications are present in the Appendix. The measured PSFs are reported in the Appendix.

4.4 In-lab Imaging

To assess the improved imaging performance of the MTF-engineered meta-optics over the forward-designed metalens, we captured imaged under broadband illumination using black-body radiation from a hotplate with high-emissivity fiberglass tape heated to 150°C as the light source. Custom aluminum targets were made using laser cutting and finished with matte black paint to prevent reflections. These targets were placed in front of the hotplate,

allowing patterned LWIR light to go through, creating contrast. A Boson 640 camera was placed on the imaging plane of the meta-optic in testing and sent the data to a PC for further post-processing, which included background subtracting, contrast stretching, and block-matching denoising. Through this predefined post-processing routine, we were able to improve the dynamic range and reduce microbolometer array artifacts.

4.5 Solving the Deconvolution Inverse Problem

Fig. 4 shows images captured in the wild with our meta-optic. In each case, we deconvolved the measurements by solving an inverse problem using a data-free image prior. Each 640×512 image was modeled as output of an implicit neural representation (INR) [31, 32] \mathcal{N}_θ with parameters θ . INRs are continuous functions that map local coordinates $(x, y$ for images) to a given output (image intensity). A unique property enabled by certain INRs, particularly ones equipped with a complex Gabor filter activation function, is the bias for images. This implies that the output tend to look more like images than noise. We leveraged this property to regularize the inverse problem. The specific inverse problem we solved is

$$\min_{\theta, K} \sum_{n=1}^N \sum_{m=1}^M \|I_{\text{obs}}(m, n) - (K * \mathcal{N}_\theta)(m, n)\|^2 + \eta_{\text{TV}} \text{TV}(\mathcal{N}_\theta(m, n)), \quad (3)$$

where I_{obs} is the observed 2D image, K is the PSF of the optical system, $\text{TV}()$ is the total variation loss function, and η_{TV} is the weight for the total variation loss. We perform a semi-blind deconvolution where we initialize K to be the analytical PSF from our simulations, and then solve for the parameters of the network and the PSF together.

LWIR sensors based on microbolometers suffer from fixed pattern noise, which causes horizontal and vertical striations. Inspired by recent work on removing fixed pattern noise in thermal images [33], we modeled it as a low-rank image. We then simultaneously solved for the fixed pattern noise, the PSF, and the parameters of the network, giving us

$$\min_{\theta, K, F} \sum_{n=1}^N \sum_{m=1}^M \|I_{\text{obs}}(m, n) - F(m, n)(K * \mathcal{N}_\theta)(m, n)\|^2 + \eta_{\text{TV}} \text{TV}(\mathcal{N}_\theta(m, n)),$$

s.t $\text{rank}(F) = r,$

where F is the fixed pattern noise. We used the recently developed wavelet implicit neural representations (WIRE) [32] for the INR architecture as it resulted in highest qualitative accuracy. An overview of the reconstruction pipeline is shown in section **Fig. 9**.

4.6 Fabrication

The meta-optics are fabricated on a 500 μm thick double-side polished silicon wafer, lightly doped with boron, giving a sheet resistivity of 1-10 $\Omega\text{-cm}$. Direct-write lithography (Heidelberg DWL 66+) defines the aperture locations in the photoresist covering the wafer surface. A 220 nm thick aluminum layer is deposited onto the patterned photoresist via electron beam evaporation (CHA Solution) and lifted off to construct the metal mask around the circular apertures, helping to reduce noise during the experiments. The wafer is coated with another photoresist and patterned with the meta-optic scatterers via direct-write lithography, aligned inside the defined apertures. The photoresist pattern of meta-optics is transferred to the bulk silicon to a depth of 10 μm by deep reactive ion etching (SPTS DRIE), utilizing its capability to etch with high aspect ratios and vertical sidewalls. After etching, the photoresist residue is stripped, and the fabricated meta-optics are ready for characterization. This process is shown on **Fig. 12** in the Appendix.

5 Appendix

5.1 Alignment Sensitivity

To study the robustness of the optimized optics with respect to the shift in the sensor plane, we conducted simulations with varying sensor distances. **Fig. 5** presents the spectral Strehl ratio for our complex meta-optics at sensor distances of 10.0 mm, 10.5 mm, and 11.0 mm. The wavelength-averaged Strehl ratios of these simulated systems are 0.0277, 0.0230, and 0.0157. It is observed that the peak of the Strehl ratio - denoting the system's highest performance - shifts towards shorter wavelengths, with an increase in the focal length. This phenomenon is governed by the principle that the wavelength of light and the focal length are inversely proportional in a meta-optics [3]. We find that even though the wavelength-averaged performance is robust against shift in the sensor plane, the individual peaks are still susceptible to the shift.

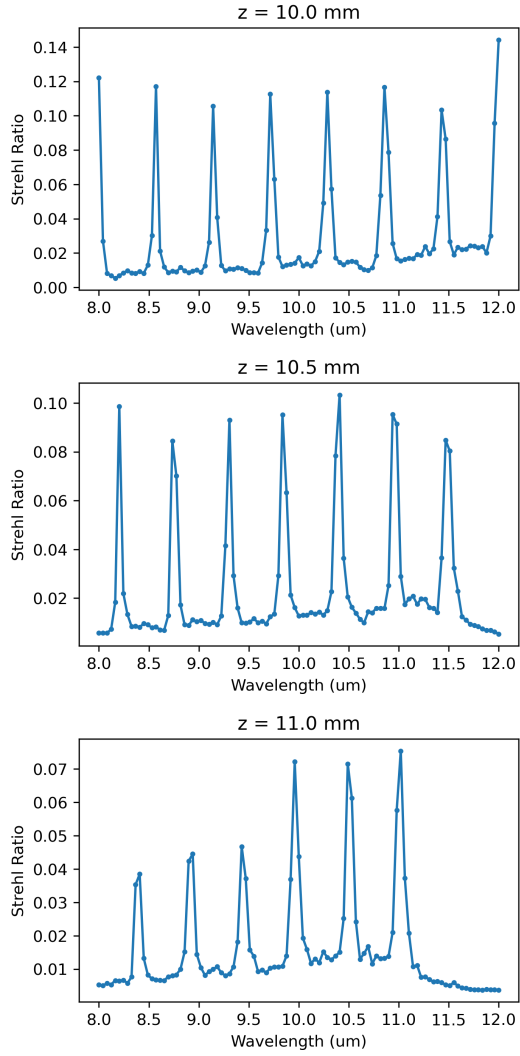


Fig. 5 The Strehl ratio of the complex meta-optic as a function of the input wavelength at different focal planes. From top to bottom, the focal lengths are 10.0, 10.5, and 11.0 mm.

5.2 PSF Characterization Results

Our initial experimental step involved measuring the point spread functions (PSFs) of the fabricated devices across various wavelengths, which can be seen in **Fig. 6**. These measurements were taken in light of the alignment sensitivity explained in Section 5.1, necessitating sparse sampling of PSFs across the spectrum at specific wavelengths—namely, 8.0, 8.5, 9.5, 10.0, and 10.5 micrometers. This selection of wavelengths was chosen to facilitate a direct comparison with simulated PSFs, thereby enabling us to validate our models effectively. It is important to note that due to the aforementioned alignment sensitivity (as discussed in Section 5.1), we deliberately refrained from capturing PSFs at the optimized wavelengths. Subsequently, the experimentally obtained PSFs were evaluated in conjunction with their corresponding modulation transfer functions (MTFs) and compared against their simulated counterparts. The experimental results displayed a strong correlation with the simulations, underlining the accuracy and reliability of our computational models.

The hyperboloid metalens performs well at only a single wavelength at 10 μm , with an extremely narrow PSF spot size and a cutoff frequency in the MTF curve of ~ 20 lp/mm, compared to a diffraction limited cutoff frequency of 100 lp/mm. Although we note that the experimental setup incurs additional aberrations from the relay optics effectively decreasing the cutoff frequency. The beam size of the hyperboloid metalens quickly broadens as the operating wavelength deviates from 10 μm showing a cutoff frequency less than 2 lp/mm for other wavelengths. This is due to the inherent chromatic aberration of the diffractive nature of the metalens [22]. In contrast, both MTF-engineered meta-optics maintain a reasonably sized focal spot throughout the entire spectrum and maintain a cutoff frequency over 5 lp/mm for all wavelengths. We emphasize this is exactly what we intended in our design: rather than optimizing for one wavelength, we wanted to have a uniform MTF over the whole wavelength range.

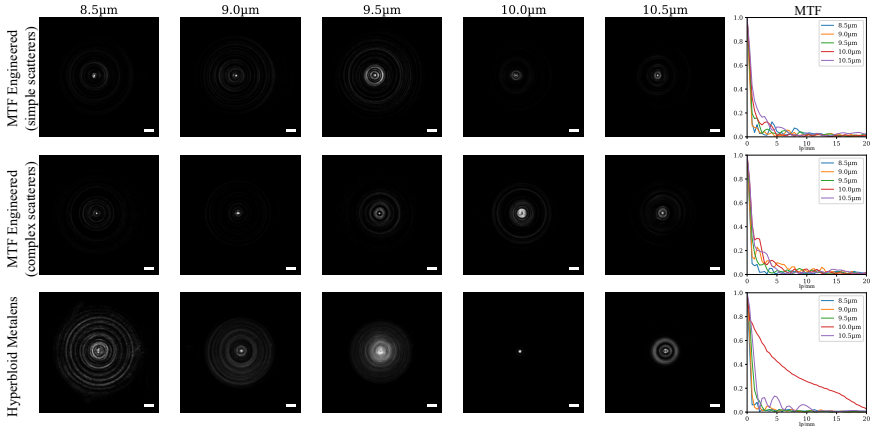


Fig. 6 PSF and MTF characterizations for the hyperboloid metalens (top), MTF engineered meta-optic with simple scatterers (middle), and MTF engineered meta-optic with complex scatterers (bottom). The scale bar is 200 μm in width.

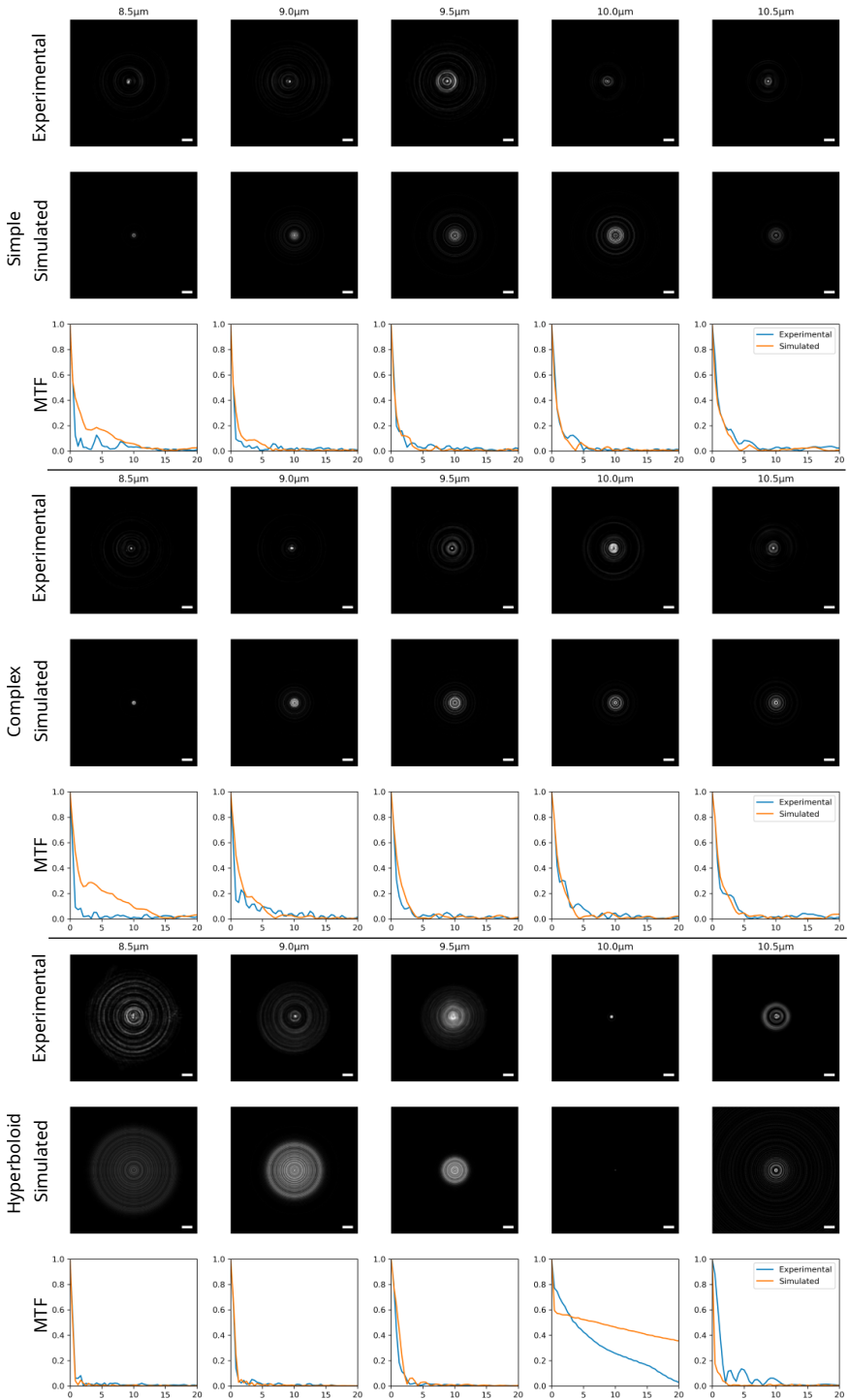


Fig. 7 Simulated vs. experimental PSFs and MTFs. Comparing between “simple”, “complex”, and hyperboloid meta-optics, from top to bottom, respectively. The scale bar is 200 μm in width.

5.3 PSF Characterization Setup

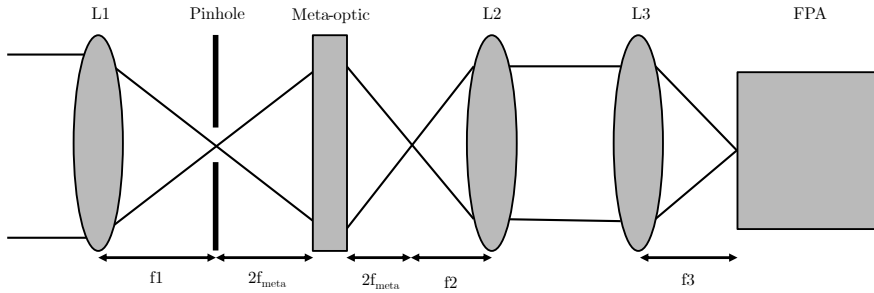


Fig. 8 Schematic of the setup used for PSF characterization of our meta-optics.

A schematic of the setup is shown on **Fig. 8**.

- Laser Source: 8.23 - 10.93 μm QCL
- L1: Ge Aspheric Lens
- Dia. = 25.4 mm, FL $f_1 = 20.0$ mm, NA = 0.63
- Pinhole: Dia. = 30 μm
- Meta: Dia. = 10 mm, FL $f_{meta} = 10$ mm
- L2: Ge Aspheric Lens
- Dia. = 25.4 mm, FL $f_2 = 15.0$ mm, NA = 0.83
- L3: ZnSe Plano-convex Lens
- Dia. = 25.4 mm, FL $f_3 = 50.8$ mm
- Camera: 15 μm pixel pitch and 640 \times 512 pixels
- Power through pinhole: 30%

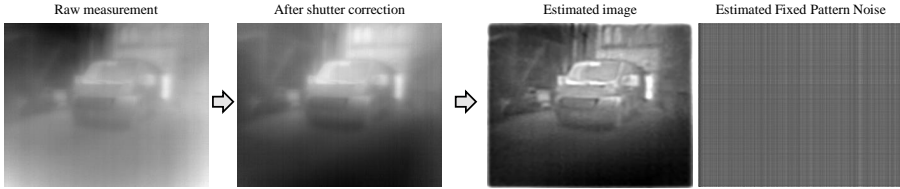


Fig. 9 Deconvolution pipeline. We used an external shutter (flat black body) to remove any internal reflections. After shutter correction, we solved an inverse problem to simultaneously estimate a sharp image, and a fixed pattern noise.

5.4 Additional Imaging Results

To demonstrate the imaging capabilities of the MTF-engineered LWIR meta-optics, in addition to the imaging results in the main text, we conducted further imaging testing “in the wild” under ambient daylight conditions, shown on **Fig. 10**. These imaging results were performed using Boson 640 camera and simple Wiener deconvolution was used. The MTF-engineered and forward-designed meta-optics were tested against a refractive lens as the ground truth. First, we imaged a vehicle parked outdoors shown on **Fig. 10(a)**. In this scene, the vehicle is clearly visible using the MTF engineered meta-optics with good details on the subject as well as the background. The hyperboloid metalens, however, does not capture the background with any fidelity, also leaving parts of the vehicle without contrast. The second series of captures on **Fig. 10(b)** show a scene of a water fountain in front of building. This series again demonstrates the increase in details via the MTF engineered meta-optic capture, allowing observers to see the trees behind the water fountain, which the hyperboloid metalens fails to demonstrate. The third series on **Fig. 10(c)** shows a woman resting against a window. The hyperboloid metalens fails to capture the subject’s glasses, which shows up on the MTF engineered case. Finally, we captured a metal “W” sculpture against vegetations in the background shown on **Fig. 10(d)**. The MTF engineered capture displays better subject separation against the background when compared to the hyperboloid metalens.



Fig. 10 LWIR imaging “in the wild”. Four scenes are imaged using the refractive LWIR lens (left), the hyperboloid metalens (middle), and the MTF engineered meta-optic with complex scatterers (right). The four scenes were all captured during daytime on a sunny day depicting (a) a parked car on a sunny day; (b) a fountain in the foreground against a building in the background; (c) a woman resting against a window; (d) a metallic structure.

5.5 Quantitative Image Analysis

To quantify the image quality, we calculate peak signal-to-noise ratios (PSNR) between the ground truth and the broadband imaging captures shown on **Fig. 3** in the main text. Each image is registered using affine transformation to eliminate potential misalignment in the captures. We present the PSNR values for the hyperboloid metalens, MTF engineered with simple scatterers, and with complex scatterers. For each device, we include three different imaging conditions – without a filter, with a $10 \pm 0.25 \mu\text{m}$ bandpass filter, and with a $12 \pm 0.25 \mu\text{m}$ bandpass filter. The PSNR values are shown on **Table 1**.

Table 1 Peak Signal-to-Noise Ratio in dB

	Hyperboloid	Simple	Complex
Broadband	11.49	10.84	13.33
Narrow-band $10 \mu\text{m}$	10.74	9.38	10.67
Narrow-band $12 \mu\text{m}$	8.26	10.02	12.65

5.6 Meta-atom Modeling

Fig. 11 presents the training loss evolution for our simple and complex meta-optic designs over multiple epochs. The models were trained using a 10-layer fully connected network (FCC) with 128 units per hidden layer and a ReLU activation function. Both models were trained using the Adam optimizer, with a learning rate set at 0.0006. The simple meta-optic design concludes training with a remarkably low loss of 0.007, while the more complex design, despite its additional intricacies, achieves an acceptable final loss of 0.048. The consistent decrease in training loss over time, seen in both scenarios, validates the robustness and effectiveness of our deep-learning assisted differentiable framework in managing the design complexities inherent in meta-optics.

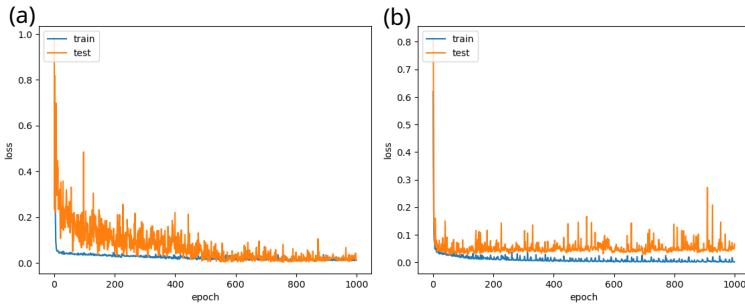


Fig. 11 Meta-optic training loss progress for the simple (a) and the complex (b) meta-atoms: each plot shows the downward trend of training loss as a function of epochs, indicating model optimization.

5.7 Fabrication Schematic

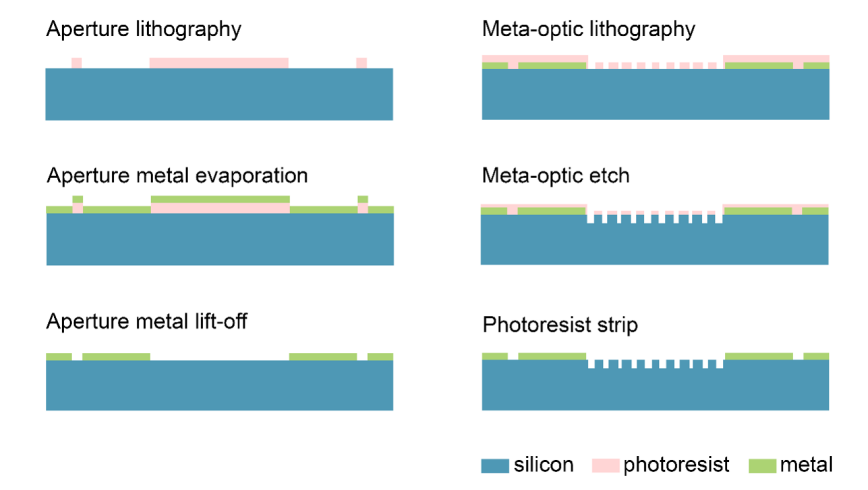


Fig. 12 Pictorial representation of fabrication process.

Funding

Funding for this work was supported by the federal SBIR program. Part of this work was conducted at a National Nanotechnology Coordinated Infrastructure (NNCI) site at the University of Washington with partial support from the National Science Foundation. J.R.H. acknowledges support from the Air Force Office of Scientific Research (Program Manager Dr. Gernot Pomrenke) under award number FA9550-20RYCOR059.

References

- [1] Vollmer, M., Möllmann, K.-P.: *Infrared Thermal Imaging: Fundamentals, Research and Applications*, pp. 88–96. John Wiley & Sons, ??? (2017)
- [2] Meem, M., Banerji, S., Majumder, A., Vasquez, F.G., Sensale-Rodriguez, B., Menon, R.: Broadband lightweight flat lenses for long-wave infrared imaging. *Proceedings of the National Academy of Sciences* **116**(43), 21375–21378 (2019). <https://doi.org/10.1073/pnas.1908447116>. Accessed 2021-03-30
- [3] Zhan, A., Colburn, S., Trivedi, R., Fryett, T.K., Dodson, C.M., Majumdar, A.: Low-contrast dielectric metasurface optics. *ACS Photonics* **3**(2), 209–214 (2016)
- [4] Arbabi, A., Briggs, R.M., Horie, Y., Bagheri, M., Faraon, A.: Efficient dielectric metasurface collimating lenses for mid-infrared quantum cascade lasers. *Optics Express* **23**(26), 33310–33317 (2015)
- [5] Farn, M.W.: Binary gratings with increased efficiency. *Applied optics* **31**(22), 4453–4458 (1992)
- [6] Lu, F., Sedgwick, F.G., Karagodsky, V., Chase, C., Chang-Hasnain, C.J.: Planar high-numerical-aperture low-loss focusing reflectors and lenses using subwavelength high contrast gratings. *Optics express* **18**(12), 12606–12614 (2010)
- [7] Arbabi, A., Horie, Y., Ball, A.J., Bagheri, M., Faraon, A.: Subwavelength-thick lenses with high numerical apertures and large efficiency based on high-contrast transmitarrays. *Nature communications* **6**(1), 1–6 (2015)
- [8] Fattal, D., Li, J., Peng, Z., Fiorentino, M., Beausoleil, R.G.: Flat dielectric grating reflectors with focusing abilities. *Nature Photonics* **4**(7), 466–470 (2010)
- [9] Aieta, F., Genevet, P., Kats, M.A., Yu, N., Blanchard, R., Gaburro, Z., Capasso, F.: Aberration-free ultrathin flat lenses and axicons at telecom

- wavelengths based on plasmonic metasurfaces. *Nano letters* **12**(9), 4932–4936 (2012)
- [10] Khorasaninejad, M., Chen, W.T., Devlin, R.C., Oh, J., Zhu, A.Y., Capasso, F.: Metalenses at visible wavelengths: Diffraction-limited focusing and subwavelength resolution imaging. *Science* **352**(6290), 1190–1194 (2016)
- [11] Banerji, S., Meem, M., Majumder, A., Sensale-Rodriguez, B., Menon, R.: Extreme-depth-of-focus imaging with a flat lens. *Optica* **7**(3), 214–217 (2020)
- [12] Arbabi, E., Arbabi, A., Kamali, S.M., Horie, Y., Faraon, A.: Multi-wavelength polarization-insensitive lenses based on dielectric metasurfaces with meta-molecules. *Optica* **3**(6), 628–633 (2016)
- [13] Arbabi, E., Arbabi, A., Kamali, S.M., Horie, Y., Faraon, A.: Controlling the sign of chromatic dispersion in diffractive optics with dielectric metasurfaces. *Optica* **4**(6), 625–632 (2017)
- [14] Colburn, S., Zhan, A., Majumdar, A.: Metasurface optics for full-color computational imaging. *Science advances* **4**(2), 2114 (2018)
- [15] Fan, Q., Liu, M., Yang, C., Yu, L., Yan, F., Xu, T.: A high numerical aperture, polarization-insensitive metalens for long-wavelength infrared imaging. *Applied Physics Letters* **113**(20), 201104 (2018)
- [16] Lin, H.-I., Geldmeier, J., Baleine, E., Yang, F., An, S., Pan, Y., Rivero-Baleine, C., Gu, T., Hu, J.: Wide field-of-view, large-area long-wave infrared silicon metalenses. *arXiv preprint arXiv:2307.12974* (2023)
- [17] Huang, L., Coppens, Z., Hallman, K., Han, Z., Böhringer, K.F., Akozbek, N., Raman, A., Majumdar, A.: Long wavelength infrared imaging under ambient thermal radiation via an all-silicon metalens. *Optical Materials Express* **11**(9), 2907–2914 (2021)
- [18] Nalbant, H.C., Balli, F., Yelboğa, T., Eren, A., Sözak, A.: Transmission optimized lwr metalens. *Applied Optics* **61**(33), 9946–9950 (2022)
- [19] Saragadam, V., Han, Z., Boominathan, V., Huang, L., Tan, S., Fröch, J.E., Böhringer, K.F., Baraniuk, R.G., Majumdar, A., Veeraraghavan, A.: Foveated Thermal Computational Imaging in the Wild Using All-Silicon Meta-Optics. *arXiv* (2022). <https://doi.org/10.48550/ARXIV.2212.06345>. <https://arxiv.org/abs/2212.06345>
- [20] Huang, L., Colburn, S., Zhan, A., Majumdar, A.: Full-color metaoptical imaging in visible light. *Advanced Photonics Research* **3**(5), 2100265

- (2022) <https://onlinelibrary.wiley.com/doi/pdf/10.1002/adpr.202100265>.
<https://doi.org/10.1002/adpr.202100265>
- [21] Presutti, F., Monticone, F.: Focusing on bandwidth: achromatic metalens limits. In: 2020 Conference on Lasers and Electro-Optics (CLEO), pp. 1–2 (2020). IEEE
- [22] Colburn, S., Zhan, A., Bayati, E., Whitehead, J., Ryou, A., Huang, L., Majumdar, A.: Broadband transparent and cmos-compatible flat optics with silicon nitride metasurfaces. *Optical Materials Express* **8**(8), 2330–2344 (2018)
- [23] Huang, L., Whitehead, J., Colburn, S., Majumdar, A.: Design and analysis of extended depth of focus metalenses for achromatic computational imaging. *Photonics Research* **8**(10), 1613–1623 (2020)
- [24] Bayati, E., Pestourie, R., Colburn, S., Lin, Z., Johnson, S.G., Majumdar, A.: Inverse designed metalenses with extended depth of focus. *ACS photonics* **7**(4), 873–878 (2020)
- [25] Lin, Z., Roques-Carmes, C., Pestourie, R., Soljačić, M., Majumdar, A., Johnson, S.G.: End-to-end nanophotonic inverse design for imaging and polarimetry. *Nanophotonics* **1**(ahead-of-print) (2020)
- [26] Campbell, S.D., Sell, D., Jenkins, R.P., Whiting, E.B., Fan, J.A., Werner, D.H.: Review of numerical optimization techniques for meta-device design. *Optical Materials Express* **9**(4), 1842–1863 (2019)
- [27] Tseng, E., Colburn, S., Whitehead, J., Huang, L., Baek, S.-H., Majumdar, A., Heide, F.: Neural Nano-Optics for High-quality Thin Lens Imaging. arXiv e-prints, 2102–11579 (2021) [arXiv:2102.11579](https://arxiv.org/abs/2102.11579) [physics.optics]
- [28] Liu, V., Fan, S.: S4: A free electromagnetic solver for layered periodic structures. *Computer Physics Communications* **183**(10), 2233–2244 (2012)
- [29] Zhelyeznyakov, M.V., Froch, J.E., Wirth-Singh, A., Noh, J., Rho, J., Brunton, S.L., Majumdar, A.: Large area optimization of meta-lens via data-free machine learning. arXiv (2022). <https://doi.org/10.48550/ARXIV.2212.10703>. <https://arxiv.org/abs/2212.10703>
- [30] Matsushima, K.: Shifted angular spectrum method for off-axis numerical propagation. *Opt. Express* **18**(17), 18453–18463 (2010). <https://doi.org/10.1364/OE.18.018453>
- [31] Sitzmann, V., Martel, J., Bergman, A., Lindell, D., Wetzstein, G.: Implicit neural representations with periodic activation functions. *Adv. Neural*

Info. Processing Systems (2020)

- [32] Saragadam, V., LeJeune, D., Tan, J., Balakrishnan, G., Veeraraghavan, A., Baraniuk, R.G.: WIRE: Wavelet Implicit Neural Representations. In: IEEE Comp. Vision and Pattern Recognition (CVPR) (2023)
- [33] Saragadam, V., Dave, A., Veeraraghavan, A., Baraniuk, R.G.: Thermal image processing via physics-inspired deep networks. In: IEEE Intl. Conf. Computer Vision (ICCV) (2021)